Tuning phase stability and short-range order through Al doping in (CoCrFeMn)$_{100-x}$Al$_x$ high-entropy alloys

Prashant Singh,[1,*] Amalraj Marshal,[2] A. V. Smirnov,[1] Aayush Sharma,[1] Ganesh Balasubramanian,[3]
K. G. Pradeep,[2,4] and Duane D. Johnson[1,5,†]

[1]*Ames Laboratory, United States Department of Energy, Ames, Iowa 50011, USA*
[2]*Materials Chemistry, RWTH Aachen University, 52074 Aachen, Germany*
[3]*Department of Mechanical Engineering & Mechanics, Lehigh University, Bethlehem, Pennsylvania 18015, USA*
[4]*Department of Metallurgical and Materials Engineering, Indian Institute of Technology Madras, Chennai 600036, India*
[5]*Department of Materials Science & Engineering, Iowa State University, Ames, Iowa 50011, USA*

For (CoCrFeMn)$_{100-x}$Al$_x$ high-entropy alloys, we investigate the phase evolution with increasing Al content ($0 \leqslant x \leqslant 20$ at.%). From first-principles theory, aluminum doping drives the alloy structurally from fcc to bcc separated by a narrow two-phase region (fcc+bcc), which is well supported by our experiments. Using KKR-CPA electronic-structure calculations, we highlight the effect of Al doping on the formation enthalpy (alloy stability) and electronic dispersion of (CoCrFeMn)$_{100-x}$Al$_x$ alloys. As chemical short-range order indicates the nascent local order, and entropy changes, as well as expected low-temperature ordering behavior, we use KKR-CPA-based thermodynamic linear response to predict the chemical ordering behavior of arbitrary complex solid-solution alloys—an ideal approach for predictive design of high-entropy alloys. The predictions agree with our present experimental findings and other reported ones.

I. INTRODUCTION

High-entropy alloys (HEAs) [1–3] continue to draw interest from the simple structures and novel properties that can appear [1,2] (mostly considered at near-equiatomic compositions) from a high configurational entropy opposing a smaller (positive or negative) formation enthalpy. So far, HEAs have been reported with body-centered cubic (bcc), face-centered cubic (fcc), and hexagonal closed-packed (hcp) [4–6] structures. With simple ground-state structures, HEAs offer a new class of materials with technologically promising properties potentially tunable using alloy design strategies, including high hardness [7], outstanding wear resistance [8], good fatigue lifetimes [9], excellent high-temperature strength [10], good thermal stability [11], and good oxidation resistance [12]. With superior radiation resistance, transition-metal-based HEAs, as compared to conventional single-phase Fe-Cr-Ni austenitic stainless steels, have attracted significant attention as high-temperature materials candidates for nuclear-energy applications [13].

Chemical complexity is a key feature of concentrated or near-equiatomic HEAs. Several studies have shown that additions of certain elements into transition-metal (TM) based HEAs can have a strong effect on the microstructure and mechanical properties [14]. With Al additions, for example, the as-cast structure tends to evolve from single fcc phase to a mixture of fcc+bcc (duplex) phase to a single bcc phase [15,16]. In particular, the effect of Al content on the structural and tensile properties of the CrMnFeCoNi system was

carefully scrutinized [17], indicating that there is a structural phase transition from fcc to bcc with increasing Al content. Similar structural transitions in Al$_x$CrCoFeNi were found experimentally [15,16] and theoretically [18,19]. Unlike conventional Fe-based alloys, alloying becomes more complex and pivotal in designing novel HEAs with desired properties. For example, phase stability and short-ranged order (SRO) in such alloys is crucial and arises from the complexity from competing pair correlations [18].

Here we present a systematic study of phase formation, structural, and magnetic stability of (CoCrFeMn)$_{100-x}$Al$_x$ HEAs resulting from variation of the% Al. For selected alloys, i.e., $x = 0$, 5, and 20 at.% Al, we predict global (formation enthalpies) and local stability (SRO) using the KKR-CPA electronic-structure method, which historically handles chemical and magnetic disorder effects well [20,21], including quantum criticality [22]. We also predict the magnetic transition temperature (CoCrFeMn)$_{100-x}$Al$_x$ HEA using mean-field estimates. The valence-electron composition (VEC) range for stable alloy phases might overlap and the range vary depending on the specific alloy. We calculate the VEC directly from the electronic structure and use it as a physical parameter controlling the fcc/bcc phase stability for solid solutions. In addition, we validate predictions with experimental results for these HEAs.

II. METHODS

A. KKR-CPA calculations

The KKR electronic-structure method is an all-electron Green's function method implemented within a scalar-relativistic approximation, i.e., spin-orbit is ignored beyond

---

*prashant40179@gmail.com
†ddj@iastate.edu; ddj@ameslab.gov

the core electrons. KKR is combined with the coherent-potential approximation (CPA) to address chemical disorder [20,23]. The screened CPA is used to address Friedel screening from configurational charge correlations [24]. Formally configurational averaging of the Green's function in KKR-CPA requires only 1 atom (2 atom) per cell for disorder alloys with fcc/bcc (hcp) structures for any arbitrary composition. Green's function integration uses a complex-energy contour on a 20-point Gauss-Legendre semicircular contour, taking advantage of analytic continuation to decrease dramatically solution times [25]. The generalized gradient approximation to exchange correlation within density functional theory (DFT) was included through use of *libXC* libraries [26]. Formation energies (E_f), electronic density of states (DOS), and electronic dispersion (Bloch spectral functions) are calculated within the atomic sphere approximation (ASA) with periodic boundary conditions (PBC) to incorporate interstitial electron contributions to Coulomb energy from all atomic Voronoi polyhedra. Brillouin zone (BZ) integrations for self-consistent charge iterations were performed with a $20 \times 20 \times 20$ Monkhorst-Pack $\boldsymbol{k}$-point mesh [27], whereas a $50 \times 50 \times 50$ mesh was used for the physical density of states (DOS) calculations. For Bloch-spectral-function (BSF), we use 300 $\boldsymbol{k}$ points along high-symmetry lines in the irreducible fcc/bcc BZ to visualize the electronic dispersion. As needed, we investigate HEAs with $3d$ magnetic elements in the paramagnetic state using the DLM (disordered local moment) approximation [28]. The DLM state, representing the state above the magnetic transition temperature (e.g., Curie temperature for ferromagnet), may have finite local moments on an atomic site that is randomly oriented (4π sr), which give zero magnetization on average over orientations. Notably, the DLM state is distinct from a nonmagnetic state (zero magnetization per site) or from an ordered configuration with collinear moments on a site that sums to zero in a supercell, which is an antiferromagnetic or ferrimagnetic, rather than a paramagnet, state.

B. Chemical SRO

From KKR-CPA thermodynamic linear response we calculate the Warren-Cowley SRO parameters for μ-ν pairs: $[\alpha_{\mu\nu}(k;T)]^{-1} = [c_\mu(\delta_{\mu\nu} - c_\nu)]^{-1}[(\delta_{\mu\nu}c_\mu^{-1} + c_N^{-1}) - (k_B T)^{-1}S_{\mu\nu}^{(2)}(k;T)]$. The $S_{\mu\nu}^{(2)}(k;T)$ is the second variation of the alloy free energy (F) with respect to composition ($c_\mu; c_\nu$) fluctuations $[\frac{\delta^2 F}{\delta c_\mu \delta c_\nu}|_0]$ evaluated in the high-T disordered phase [18,29]. The free energy (F) of the solid-solution encompasses electronic effects such as hybridization, band filling, and Fermi-surface nesting [28]. For a specific wave-vector instability ($\boldsymbol{k_o}$) at the spinodal temperature T_{sp}, $\alpha_{\mu\nu}^{-1}(\boldsymbol{k_o}; T_{sp})$ vanishes, signifying an absolute instability to this chemical fluctuation and estimates the order-disorder or miscibility gap temperature [18,29–32]. The dominant SRO pairs are identified above T_{sp} from the stability matrix $S_{\mu\nu}^{(2)}(\boldsymbol{k};T)$ and reveals the unstable (Fourier) modes with ordering wave vector $\boldsymbol{k_o}$, or phase separation (clustering) at $\boldsymbol{k_o} = (000)$. Hence, we can determine from the stability matrix which wave vector first goes unstable and what pair(s) drive this instability. At T_{sp}, the phase change is driven by one of the pairs in chemical stability

matrix "$S_{\mu\nu}^{(2)}(\boldsymbol{k}; T)$." Such information is crucial in predicting SRO in solid-solution alloys. For $N > 2$, pairs driving ordering (clustering) will not necessarily be the same pairs that peak in the SRO parameters $\alpha_{\mu\nu}(k)$ due to the abeyance of the optical theorem (or particle conservation) [32].

Currently, the SRO is coded in the approximate ASA formalism, so the KKR-CPA-ASA is used for all $S_{\mu\nu}^{(2)}(\boldsymbol{k}; T)$ calculations. This ASA-only formalism neglects differences in interstitial Coulomb energy that vary with crystal structure and is a source of discrepancy for SRO temperature scale. As the pairwise chemical interchange energies $S_{\mu\nu}^{(2)}(\boldsymbol{k}; T)$ do not give direct spatial pair correlations, we inverse Fourier transform $S_{\mu\nu}^{(2)}(\boldsymbol{k})[=S_{\mu\nu,0}^{(2)} + \sum_n \sum_{\mu\nu} S_{\mu\nu,n}^{(2)} e^{i\boldsymbol{k}.\boldsymbol{R_n}}]$ to real space to further evaluate the real-space Warren-Cowley SRO.

C. Curie temperature estimate

In ordering systems, energy difference mainly determines the transition temperature [33]. Thus, to assess the Curie temperature (magnetic ordering), we consider a Heisenberg-like model in mean-field theory [34] and find that $T_c = \frac{2}{3}[E_{DLM} - E_{FM}]/k_B$, proportional to the energy difference between PM (DLM) and FM states. Sometimes, as in a dilute magnetic semiconductor [34], it is appropriate to consider a nonmagnetic element with concentration c and, as such, the relation is slightly modified to $T_c = \frac{2}{3}[\frac{1}{1-c}][E_{DLM} - E_{FM}]/k_B$, which serves here as an upper bound.

D. Materials preparation and characterization

CoCrFeMnAl-based HEAs with Al concentrations (0, 5, and 20 at.% Al) were synthesized by arc melting of high purity ($\geqslant 3N$) metal powders of Co, Cr, Fe, Mn, and Al, under an Ar atmosphere. To ensure homogeneity, the alloys were remelted five times prior to casting in copper molds. The crystal structure of each sample was determined by x-ray diffraction (XRD) using Cu-$K\alpha$ radiation. A Siemens D5000 diffractometer operating in Bragg Brentano geometry at 40 kV was used to obtain the diffractograms. Alloy microstructure and the corresponding surface chemical distribution were mapped using a Zeiss SIGMA^{TM} field-emission scanning electron microscope (FE-SEM) equipped with an Oxford X-maxN^{TM} energy-dispersive x-ray spectroscopy (EDX) detector. An electron accelerating voltage of 20 kV was used, and the chemical quantification was performed considering only the $K\alpha$ x rays. Electron back scattered diffraction (EBSD) was performed to further verify phase formation and to visualize the microstructure along with their grain orientations. A Zeiss LEO 1530 FE-SEM with an EBSD detector was used for this purpose and the analysis of EBSD data was performed with AZtecHKL software. The thermal stability of the HEAs was investigated using a NETZSCH STA 449C differential scanning calorimeter (DSC). The heating and cooling curves were recorded at a reduced rate of 5 K/min until 1500 °C in an Ar atmosphere. A local electrode atom probe (LEAP 4000X HR^{TM}) was used to study the three-dimensional elemental distribution on a near-atomic scale. The samples for atom probe tomography (APT) were prepared using a FEI Helios Nanolab 660 dual beam workstation. APT measurements were performed at the set temperature
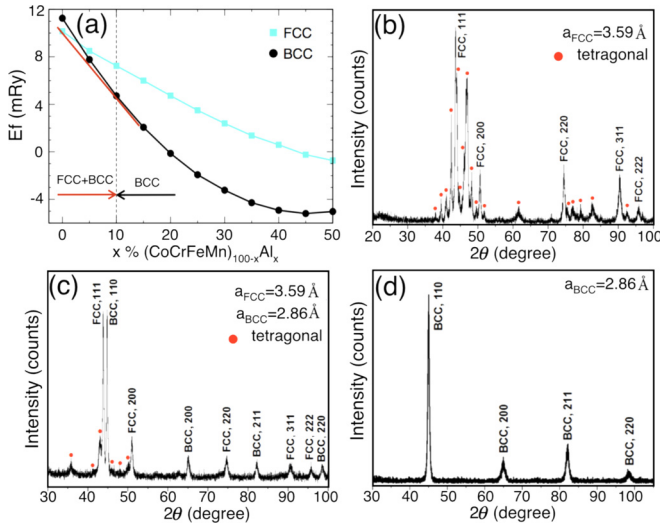
FIG. 1. (a) Formation energy (mRy/atom) versus at.% Al in fcc and bcc $(CoCrFeMn)_{100-x}Al_x$. Common tangent line (red line) highlights mixed (fcc + bcc) phase for $x < 10$ at.% Al. Adding more Al stabilizes the bcc phase. XRD pattern of the as-cast $(CoCrFeMn)_{100-x}Al_x$ for (b) $x = 0$, (c) $x = 5$, and (d) $x = 20$ at.% Al.

of 60 K in the laser pulsing mode, with an applied pulse energy and frequency of 30 pJ and 250 kHz, respectively. APT data reconstruction and analysis were carried out using IVAS 3.6.10a software provided by Cameca Instruments.

III. RESULTS AND DISCUSSION

A. Phase formation and structural stability

We predict phase stability of $(CoCrFeMn)_{100-x}Al_x$ HEAs from the total-energy calculations of potential ground-state structures and find the minimum via the formation enthalpies. Previous theoretical and experimental observations show that small Al doping to TM-HEAs promotes the formation of stable fcc/bcc/duplex phases [3,18]. The Al addition is also found to increase the equilibrium volume of the solid solution, consistent with the fact that atomic radii of Al is larger than those of the other elemental components.

We show phase stability in Fig. 1(a) for the fcc/bcc phase of $(CoCrFeMn)_{100-x}Al_x$ at 0 K. We find that the fcc phase is stable at $x = 0$ at.% Al, a two-phase region (fcc+bcc) is lowest in enthalpy for $0 < x \leqslant 10$ at.% Al ("Al-poor" region), and bcc is stable for $x > 10$ at.% Al ("Al-rich" region). In Fig. 1(a) it is clear that the structural energy difference between ideal fcc and bcc lattices vanishes at $x \approx 4$ at.% Al. However, the common tangent to the formation enthalpy curves establishes that there is a two-phase (fcc+bcc) region ($x < 10$ at.% Al) that lowers the overall enthalpy of the homogenous system into a weighted mixture of two phases, where (fcc+bcc) equilibria may occur when the chemical potentials of the two phases become equal. These predictions are compared to experimental results of $(CoCrFeMn)_{100-x}Al_x$ at 0, 5, 20 at.% Al, see Figs. 1(b)–1(d) XRD pattern. We observe predominant peaks in Fig. 1(b) for 0% Al corresponding to fcc. A tetragonal phase (Cr-based, as per ICDD JCP2 database

PDF 09-0052, 05-0708) was also identified. In Fig. 1(c) for 5 at.% Al, similar to CoCrFeMn, multiple phases including fcc and a tetragonal phase (Cr-based, as per ICDD JCP2 database) were observed along with a secondary bcc phase. However, the XRD pattern [Fig. 1(d)] of equiatomic CoCrFeMnAl (i.e., 20 at.% Al) clearly shows single bcc phase. The role of Al in stabilizing the bcc phase was similar to the many reports for Al-containing HEA, where bcc is stabilized with increasing% Al [28,35–40].

Focusing on $(CoCrFeMn)_{100-x}Al_x$ at $x = 0$ at.% Al with single fcc phase, at $x = 5$ at.% Al (Al-poor region) exhibiting two-phase (fcc+bcc), and at $x = 20$ at.% Al (Al-rich region) with single bcc phase, we calculate each alloy's electronic structure and short-range order, and compared with our experimental results. The calculated lattice constants for $(CoCrFeMn)_{100-x}Al_x$ are 3.54 Å (fcc) at 0 at.% Al, 3.55 Å (fcc) and 2.83 Å (bcc) at 5 at.% Al, and 2.84 Å (bcc) at 20 at.% Al, which agree well with our experimental findings of 3.59 Å (0 at.% Al, fcc), 3.58 Å (5 at.% Al, fcc), 2.86 Å (5 at.% Al, bcc), and 2.86 Å (20 at.% Al, bcc), respectively. Although changing Al concentration shows very little effect on lattice constants (either calculated or experiment), the calculated bulk modulus reduces significantly from 247.1 GPa at 0 at.% Al, to 218.3 (fcc)/209.1 (bcc) at 5% Al, and to 169.5 GPa at 20% Al. This happens because Al additions reduce the alloy's interstitial electron number (electronic density) [41], which controls the moduli. The calculations at 0 K are helpful to understand, characterize, and predict mechanical properties [18] and enables selection of materials for further studies.

B. Magnetic stability

For $(CoCrFeMn)_{100-x}Al_x$ we address nonmagnetic (NM), paramagnetic (PM) within the DLM approximation [26], and ferromagnetic (FM) states. For 0% Al, fcc CoCrFeMn has a NM ground state that is energetically more stable than DLM and FM. Alloying with at.% Al, CoCrFeMn HEA becomes magnetic and DLM or FM phase is lower in energy than NM phase. For 5% Al, DLM phase is energetically more stable than NM or FM phase. In DLM phase, Fe/Mn/Co possess nonzero site moments. Increasing from 0 to 5 at.% Al [Fig. 1(a)], the alloy shows a mixed (fcc+bcc) phase, so we analyze magnetic behavior of both fcc and bcc phases. In fcc phase, only Fe possesses small DLM moment of 0.52 μ_B, while in bcc phase Fe/Mn/Co shows DLM moment of 2.02/0.92/1.00 μ_B. For 20 at.% Al (equiatomic case), the alloy forms single bcc phase, with DLM moment on Fe/Mn/Co reduced slightly to 1.91/0.98/0.79 μ_B relative to 5 at.% Al bcc phase, and average total local moment of 0.74 μ_B at 0 K, with net zero magnetization. The experimentally measured total magnetization of the equiatomic CoCrFeMnAl BCC-stabilized HEA is 0.58 μ_B at 50 K (0.45 μ_B at 300 K). With increasing at.% Al, $(CoCrFeMn)_{100-x}Al_x$ undergoes a transition from NM-fcc to DLM/FM-(fcc+bcc) to FM-bcc state. The at.% Al has a strong impact on the magnetic behavior of the HEA.

To assess the Curie temperature (T_c) we consider differences in the total energy/atom for DLM E_{DLM} and FM E_{FM} states. In contrast to segregating systems [42], the transition
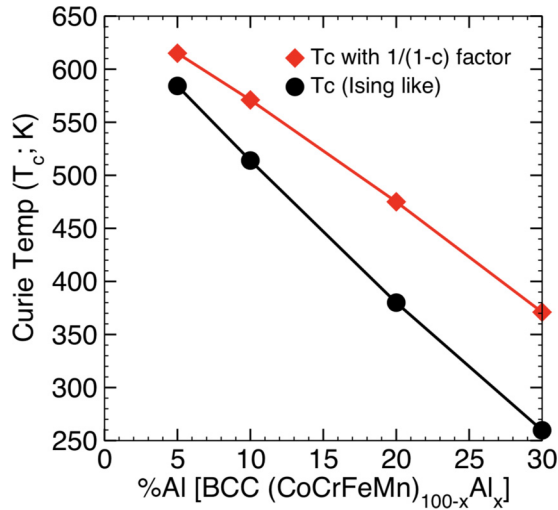
FIG. 2. Curie temperatures versus at.% Al for bcc $(CoCrFeMn)_{100-x}Al_x$ estimated from mean-field approximation [30–32], see Sec. II.

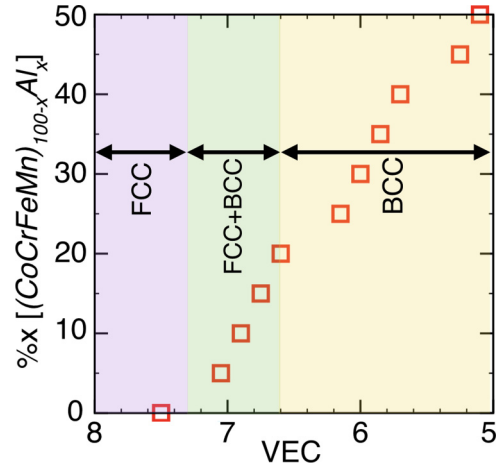FIG. 3. Relationship between valence electron composition (VEC) and phase stability of the fcc and bcc phases of $(CoCrFeMn)_{100-x}Al_x$ HEA.

temperature in ordering systems (with negative formation enthalpies) are dictated mainly by energy differences [33]. Thus, for magnetic ordering, mean-field theory gives an estimated $T_c = \frac{2}{3}[E_{DLM} - E_{FM}]/k_B$, where k_B is Boltzmann's constant. For equiatomic bcc-CoCrFeMnAl, the calculated $E_{DLM} - E_{FM}$ is 3.61 mRy, giving $T_c = 380$ K(107 °C). In Fig. 2 for bcc $(CoCrFeMn)_{100-x}Al_x$ we plot the estimated T_c versus $x\%$ Al ($x = 5$–30% Al) [34] and include an upper bound (see Sec. II).

C. Valence electron count (VEC)

The VEC is found self-consistently in our electronic-structure calculations and obtained by integrating the density of states (DOS) of the valence states over occupied states (up to the Fermi energy E_F). VEC is correlated directly to the stability of fcc or bcc phases. To best of our knowledge, in solid-solution HEAs, there are no exceptions to the trend that a higher VEC favors the fcc and a lower VEC favors the bcc. This can be justified as follows: bcc forms for $4 <$ VEC < 6 [3,29], as stability increases when bonding d states fill and maximal when half-filled (VEC~6); antibonding states fill roughly when VEC > 6 and stability decreases. For $6.8 <$ VEC < 8 other phases compete (e.g., σ phase), and fcc becomes stable for VEC > 8 [3,29]. The threshold VEC values of 6.87 and 8.0 is a reasonable guide to stabilize fcc or bcc HEAs. In the $(CoCrFeMn)_{100-x}Al_x$, fcc HEA is more stable than bcc at a VEC ~ 7.5 ($x = 0$ at.% Al), while bcc stabilizes at VEC $= 6.6$ ($x = 20$ at.%), see Fig. 1(a). Hence, an fcc+bcc phase exists at an intermediate VEC (e.g., 7.275 at $x = 5$ at.% Al), although the formation enthalpy is still positive. Thus, we see roughly the same VEC limit for $(CoCrFeMn)_{100-x}Al_x$ as the empirically defined solid-solution phase limit, with exceptions already noted for Mn-containing HEAs [3]. We also plot the VEC for $(CoCrFeMn)_{100-x}Al_x$ [$x(Al) = 0$ to 40%] in Fig. 3. For $(CoCrFeMn)_{100-x}Al_x$, empirical and first-principles analysis correlate well in predicting relative phase

stability, which is not always the case, as in refractory alloys [29].

To shed more light on the effect of Al doping on electronic structure in an alloy (Fig. 4), we show configurationally averaged DOS and electronic dispersion (BSF) for fcc and bcc $(CoCrFeMn)_{100-x}Al_x$ at 0, 5, and 20 at.% Al. For fcc
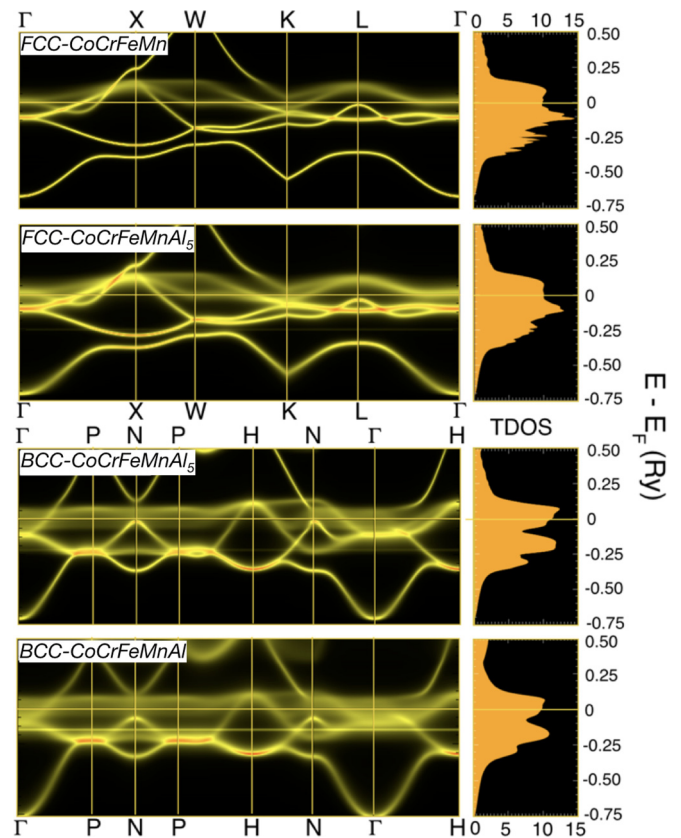

FIG. 4. For $(CoCrFeMn)_{100-x}Al_x$ at $x = 0$, 5, 20 at.% Al, the electronic dispersion (left) from the Bloch-spectral function along high-symmetry directions of fcc and bcc Brillouin zone, and (right) total density of states [states/(Ry atom spin)].
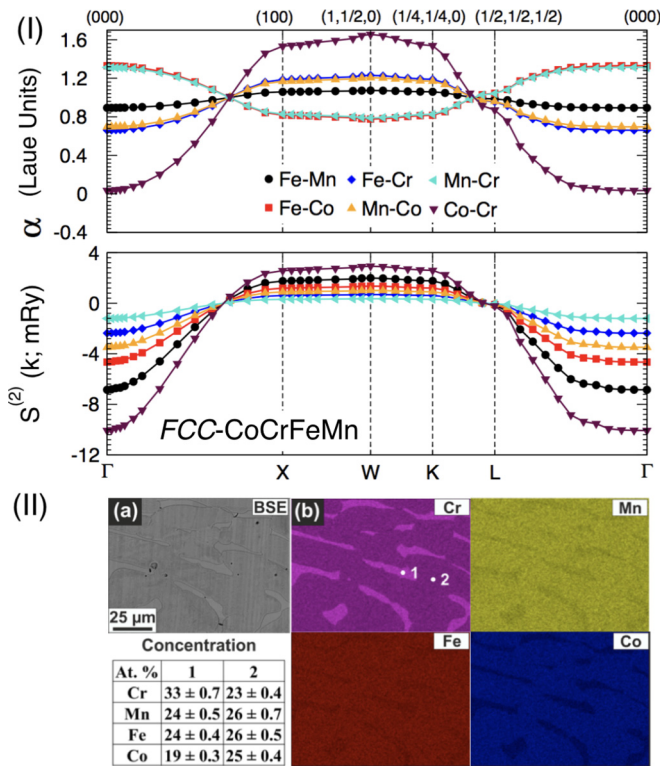
FIG. 5. (I) For equiatomic fcc CoCrFeMn, (top) Warren-Cowley SRO $\alpha_{\mu\nu}(\mathbf{k}; 1.15T_{\text{sp}})$ with $T_{\text{sp}} = 315$ K (42 °C) and (bottom) pair interchange energies, $S^{(2)}_{\mu\nu}(\mathbf{k}; 1.15T_{\text{sp}})$ plotted along high-symmetry directions of the Brillouin zone (Γ-X-W-K-L-Γ). SRO ordering instability at $W = (1, 1/2, 0)$ is driven by Co-Cr in $S^{(2)}_{\text{Co-Cr}}(W)$, however, closely competing pairs (Fe-Co; Mn-Cr) peak in the observable $\alpha_{\mu\nu}(\Gamma)$. The SRO peak at W indicates a low-temperature (below $T_{\text{sp}} = 315$ K) tetragonal phase (DO_{22}), also observed in our experiments, see Fig. 1(b). (II) (a) BSE microstructure and (b) corresponding EDX maps of CoCrFeMn. Composition of selected spots (1 and 2) in the microstructure is in the inset table.

CoCrFeMn, the DOS and BSF exhibit sharp structure at lower (filled) energies, similar to that of a pure metal. For 5 and 20 at.% Al, the alloys show disorder broadening both near and far from the E_F due to chemical and magnetic disorder for enhanced scattering accompanied with increased% Al, where DOS shows less structure. Clearly, in Fig. 4, the deep lying states move with increased at.% Al, which shows hybridization between Al s states and Fe/Co/Cr bonding $3d$ states. The shift in dispersion well below E_F (easily seen in the low-energy s states) also indicates enhanced stability of the alloy due to lowering states in energy from hybridization with Al. In (CoCrFeMn)$_{100-x}$Al$_x$, Al works as a bcc stabilizer by hybridization/band filling that enhances disorder and lowers bonding states [18]. For equiatomic HEA (20 at.% Al), see Fig. 1(a), the negative formation energy indicates the favorability for elements to mix, in contrast to the alloys with lower Al concentration (0 and 5 at.% Al), which shows segregation.

D. Short-range order

For fcc-CoCrFeMn (0 at.% Al), in Fig. 5(I), we plot the chemical interchange energies [$S^{(2)}_{\mu\nu}(\mathbf{k}; T)$] and
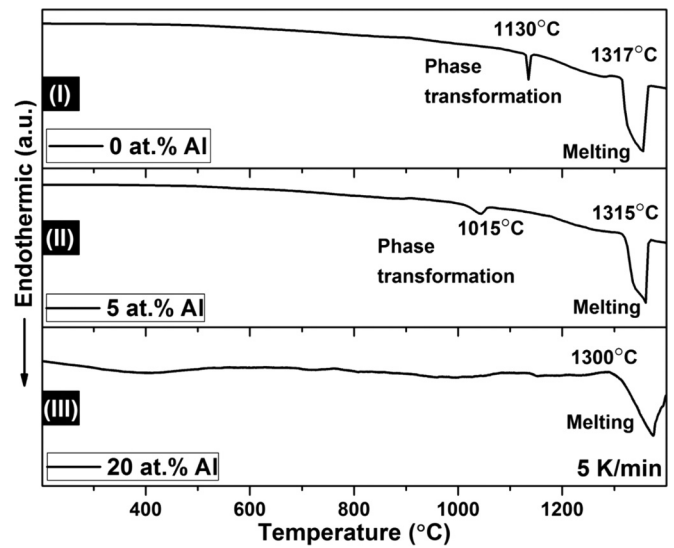

FIG. 6. DSC trace of (CoCrFeMn)$_{100-x}$Al$_x$ for x: (I) 0, (II) 5, and (III) 20 at.% Al (from Ref. [35]).

Warren-Cowley SRO parameters [$\alpha_{\mu\nu}(\mathbf{k}; T)$] at $1.15T_{\text{sp}}$ of the calculated spinodal temperature [$T_{\text{sp}} = 315$ K (42 °C)]. At T_{sp} for a specific ordering instability, the inverse pair correlation ([$\alpha_{\mu\nu}(\mathbf{k})]^{-1}$) first vanishes [i.e., $\alpha_{\mu\nu}(\mathbf{k})$ diverges]. The maximal SRO peaks of $\alpha_{\mu\nu}(\mathbf{k})$ in Fig. 5(I) at $\mathbf{k} = \{1, 1/2, 0\}$ (W points) indicates the type of ordering in CoCrFeMn HEA. At T_{sp}, particular elements of $\alpha_{\mu\nu}(\mathbf{k})$ become unstable (diverge) and indicate instability to long-range order [18]. $S^{(2)}_{\mu\nu}(\mathbf{k}; T)$ at T_{sp}, in Fig. 5(I) determines the wave-vector instability, i.e., the pair(s) driving the instability, and T_{sp} at which the instability occurs. This instability in $\alpha_{\mu\nu}(\mathbf{k})$ is related to the peak in the stability matrix $S^{(2)}_{\mu\nu}(\mathbf{k}; T)$ in select pairs, which characterizes the SRO in any arbitrary, complex solid solution. In Fig. 5(I) the $S^{(2)}_{\mu\nu}(\mathbf{k}; T)$ shows a very weak Co-Cr peak at $\mathbf{k}_0 = W = \{1, 1/2, 0\}$ in the fcc Brillouin zone, which indicates a very low-temperature (below $T_{\text{sp}} = 315$ K) tetragonal phase (DO_{22}). The tetragonal phase is observed as secondary phase in XRD measurements [Fig. 1(b)]. The peaks in $\alpha_{\mu\nu}(k)$ at Γ (000) has a dominant competing segregation peaks in Fe-Co and Mn-Cr pairs. Furthermore, Fe-Mn, Fe-Cr, and Mn-Co pairs show flat weights, indicating tendency of equal probability of mixing. The Co-Cr SRO with peak at $W = (1\,1/2\,0)$ indicates the tendency of Cr to enrich over Co, i.e., Cr-Co pair shows ordering tendency and Cr preferably occupies sites around Co in the low-T tetragonal phase. Experiments [Fig. 5(II)] indicate the presence of a secondary tetragonal phase due to phase decomposition.

In Fig. 5(II)(a) we show the BSE image of the 0 at.% Al alloy representing the phase-separated microstructure. The presence of two-phase regions (inferred from the phase contrast) is consistent with the XRD results in Fig. 1(b). EDX mapping of the corresponding area, Fig. 5(II)(a), reveal regions (1 and 2) with different chemical concentration, where region 1 has larger% Cr than the region 2. The quantification of these two chemically distinct regions is given in inset of Fig. 5. The Cr-rich region (1) has $\sim$33 at.% Cr, with constant Mn and Fe concentrations ($\sim$24 at.% each), and was found to be depleted in Co. In contrast, region 2 ($\sim$23 at.% Cr) was richer
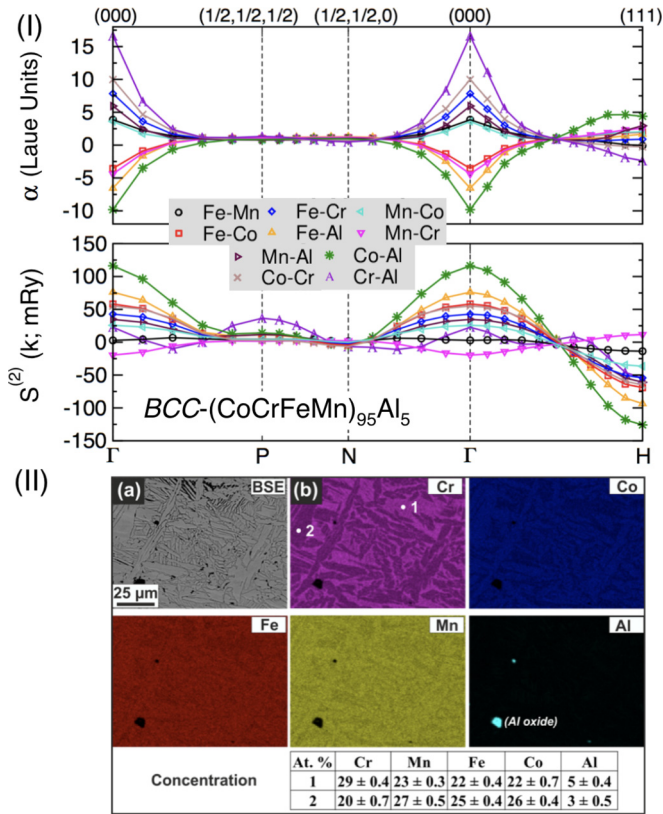
FIG. 7. (I) For bcc $(CoCrFeMn)_{95}Al_5$, (top) Warren-Cowley SRO $\alpha_{\mu\nu}(k; 1.15T_{sp})$ with $T_{sp} = 1410$ K (1137 °C) and (bottom) pair interchange energies, $S^{(2)}_{\mu\nu}(k; 1.15T_{sp})$ along high-symmetry directions of Brillouin zone (Γ-P-N-Γ-H). The Γ-mode (000) clustering instability is driven by Cr-Al in $S^{(2)}_{Cr-Al}$ (Γ), and manifested by Co-Al peak in $\alpha_{Co-Al}(\Gamma)$. The probability sum rule [32] shows Co-Al as the dominant SRO pair in $\alpha_{Co-Al}(\Gamma)$, while chemical stability matrix $S^{(2)}_{Cr-Al}$ (Γ) shows Cr-Al as driving pair at T_{sp}. (II) (a) BSE microstructure and (b) corresponding EDX maps of the 5 at.% Al HEA. Composition of selected regions (1 and 2) in the microstructure is shown in the inset table. Dark spots in (a) correspond to (Al) oxide inclusions.

in Mn, Fe, and Co. Similar separation of the Cr-based phase has been widely reported in other Cr-containing transition-metal-based HEAs [17,35,43]. The observed phase separation phenomenon is in good agreement with calculated SRO, see Fig. 5(I). The SRO peak at W indicates the possibility of low-temperature tetragonal phase [also see Fig. 1(b)]. The thermal stability analysis of the multiphase CoCrFeMn HEA is shown in Fig. 6(I). An endothermic peak (at 1130 °C) in addition to the solid-liquid phase transition (peak at 1317 °C) potentially corresponds to the decomposition of the observed Cr-rich phase (spinodal decomposition). Our mean-field estimate of the miscibility gap $T_{MG} = \Delta E_f/\Delta S_{conf} \sim 10.3$ mRy$/k_B \ln 4 \sim 1174$ K (901 °C) is similar to DSC measurements (1130 °C).

Notably, however, the SRO-predicted T_{sp} of 315 K (42 °C) for fcc CoCrFeMn deviates from that found directly from the enthalpy estimate 1174 K (901 °C) (where they should agree). We have tracked this discrepancy partly to the variations of the ASA-only free energy used to estimate the SRO response functions (which will be corrected in the future by including
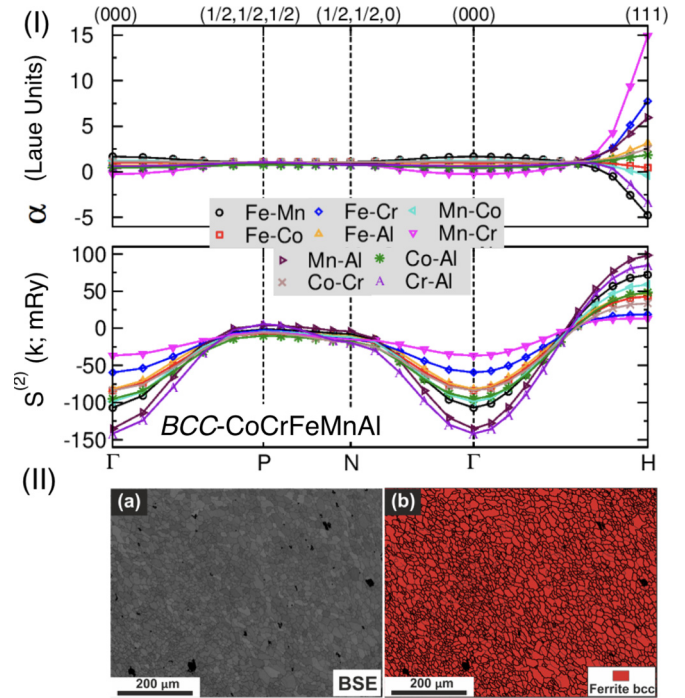

FIG. 8. (I) For equiatomic bcc CoCrFeMnAl, (top) Warren-Cowley SRO $\alpha_{\mu\nu}(\boldsymbol{k}; 1.15T_{sp})$ with $T_{sp} = 1360$ K (1087 °C), and (bottom) pair interchange energies, $S^{(2)}_{\mu\nu}(\boldsymbol{k}; 1.15T_{sp})$ along high-symmetry directions of Brillouin zone (Γ-P-N-Γ-H). H-mode [111] ordering instability is driven by Mn-Al in $S^{(2)}_{Mn-Al}(H)$, and manifested by Cr-Mn peak in $\alpha_{Cr-Mn}(H)$. (II) For CoCrFeMnAl, (a) BSE microstructure and (b) EBSD phase map.

contributions from interstitial Coulomb energy with cell shape and periodicity). Along with the ASA, the complex nature of Mn-$3d$ bands also contributes in the underestimation of transition temperature. For equiatomic FeMnCoCr HEA, see Fig. 3, the VEC (7.5) from integrated density of states, slightly lower than actual VEC (8) [3]. The discrepancy mostly results in a decrease of the spinodal temperature in the fcc phase, and fortunately has less effect on the bcc phase. In short, the competing phase separating (clustering) (Γ) and weak ordering (W) seen in SRO in Fig. 5(I) shows qualitative agreement with experiments.

For bcc $(CoCrFeMn)_{95}Al_5$ in Fig. 7(I), $S^{(2)}_{\mu\nu}(\boldsymbol{k}; T)$ and $\alpha_{\mu\nu}(\boldsymbol{k})$ have peaks at $\boldsymbol{k}_0 = \Gamma = [000]$ in the bcc Brillouin zone, indicative of phase separation (infinite wavelength fluctuation). $\alpha_{\mu\nu}(\Gamma)$ has a dominant SRO peak in Cr-Al (followed by Co-Cr and Fe-Cr); however, the phase separation is actually driven by the Co-Al pair in $S^{(2)}_{\mu\nu}(\boldsymbol{k}; T)$. Figure 7(II)(a) shows the multiphase microstructure of the 5% Al HEA, which consists of a lamellar grain morphology. The corresponding elemental mapping by EDX of the same region reveals Cr-rich and Cr-depleted regions, see Fig. 6(II)(b), similar to the CoCrFeMn. The Cr-rich region had $\sim$29 at.% Cr, with constant% Mn, Fe, and Co of $\sim$22 at.%. The Cr-depleted region had $\sim$20 at.% Cr with $\sim$25 at.% Mn, Fe, and Co, slightly higher than the Cr-rich region. Whereas the maximum% Al was partitioned to the Cr-rich region. The observed instability to phase separation at the 5 at.% Al is in good agreement with our predictions. The thermal stability
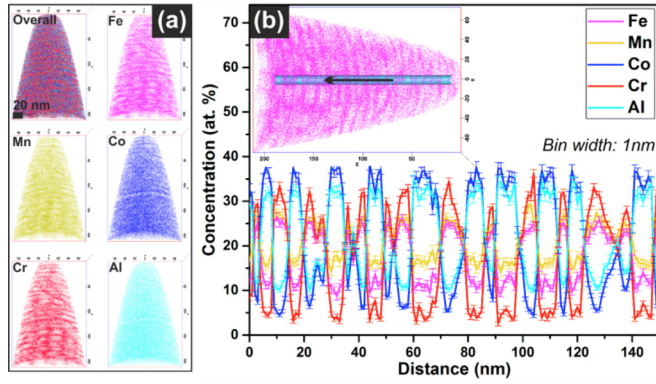
FIG. 9. For CoCrFeMnAl, APT analysis showing (a) three-dimensional reconstruction of Co, Cr, Fe, Mn, and Al atom positions. (b) One-dimensional concentration profile of the alloying elements taken along a cylinder (shown in the inset) of 10 nm diameter with 1 nm bin width.
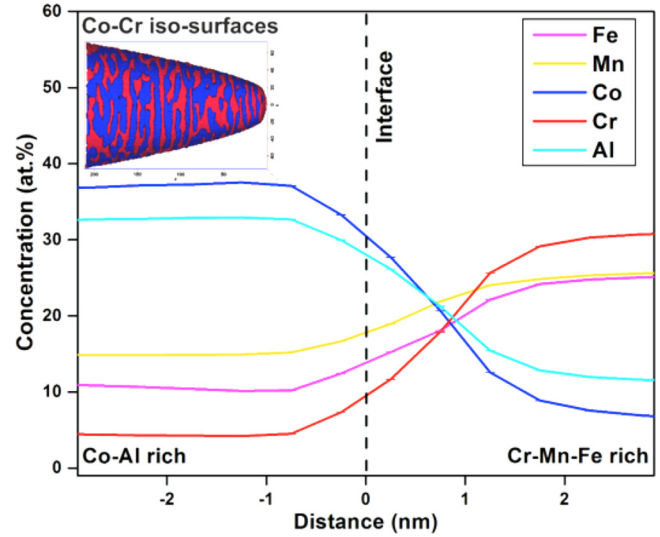

FIG. 10. APT analysis of CoCrFeMnAl showing isosurfaces highlighting the 30 at.% Co and 20 at.% Cr regions (inset), and the corresponding proximity histogram of 0.5 nm bin width across the separating phases.

evaluation of the phase separated 5 at.% Al HEA is shown in Fig. 7(II). The measured DSC curve shows a prominent endothermic peak along with the melting peak, similar to one observed for CoCrFeMn HEA in Fig. 6(I). The phase transformation could be due to decomposition into the observed Cr-rich and Cr-poor regions. In contrast to 0 and 5% Al cases, equiatomic bcc CoCrFeMnAl shows peak in $S^{(2)}_{\mu\nu}(\mathbf{k}; T)$ and $\alpha_{\mu\nu}(\mathbf{k})$ at $\mathbf{k}_0 = H = [111]$, see Fig. 8(I). Clearly the Mn-Al pair drives the instability as shown in $S^{(2)}_{\mu\nu}(\mathbf{k}; T)$, however, the SRO has dominant peak in Mn-Cr. The apparent oddity (but correct) in different chemical pairs in $S^{(2)}_{\mu\nu}(\mathbf{k}; T)$ and the SRO in multicomponent alloys arises from the probability sum rule (or optical theorem for particle conservation) [32].

The microstructure of the equiatomic HEA is displayed in Fig. 8(II)(a). Equiaxed grains with an average grain size of ∼10 μm were observed. The EBSD phase mapping in Fig. 8(II)(b) of the corresponding area indicates the presence of single bcc phase. This further affirms calculated phase stability predictions and XRD observations in Figs. 1(a) and 1(d). No indication of phase separation was observed in the EDX mapping (not shown here). However, atomic-scale investigation by APT reveals nanoscale chemical separation in the analyzed volume of $145 \times 147 \times 212\,\mathrm{nm}^3$ [see Fig. 9(a)], where Co- and Cr-rich regions were seen. Corresponding one-dimensional concentration profile taken along a cylindrical region of interest, $10 \times 10 \times 180\,\mathrm{nm}^3$ along the tip length, shows anticorrelated fluctuations between Cr-Mn-Fe and Co-Al elements [Fig. 9(b)]. Even though anticorrelated fluctuations are characteristics of spinodal decomposition [36], DSC curves reported for equiatomic CoCrFeMnAl in

Fig. 6(III) had no signs of phase transition until the melting point. Figure 10 (inset) shows isoconcentration surfaces of Co and Cr, an intertwined morphology was observed between the Cr- and Co-enriched regions. Proxigram extending from Co-rich to Cr-rich region across the interface was plotted (Fig. 10) to determine the actual chemical composition of the separating phases. The Cr-rich region had a composition of $Co_7Cr_{31}Fe_{25}Mn_{25}Al_{12}$, while the concentration of the Co-rich region was $Co_{38}Cr_4Fe_{25}Mn_{25}Al_{33}$.

The SRO in Fig. 8(I) shows peak at H [111] with Cr-Mn as dominant pair in CoCrFeMnAl. The peak at H point indicates the possibility of $B2$-type ordering. While no $B2$ ordering was observed in our XRD data [Fig. 1(d)], a recent work on an equiatomic single crystal reports $B2$-type ordering [37]. The synthesis of a single crystal involved extremely low cooling rates and resulted in the formation of nearly equilibrium phase; the Cr-rich region was disordered bcc and the Co-Al-rich precipitates were ordered $B2$, embedded in the disordered bcc matrix [37]. The two-phase structure is thus similar to that found in equiatomic AlCoCrFeNi [36]. The bcc/$B2$ coherent morphology is closely related to the lattice misfit between these two phases, which is induced by the spinodal decomposition at higher Al content. The calculated SRO shows spinodal decomposition driven by the strongest SRO pair Mn-Cr, see Fig. 8(I), giving phase decomposition at T_{sp}. The Mn-Cr-rich phase observed by experiments, further

TABLE I. Summary of phase stability and SRO predictions by KKR-CPA and experimental observations for the $(CoCrFeMn)_{100-x}Al_x$.

HEA →	0 at.% Al	5 at.% Al	20 at.% Al
Calculated phase stability	fcc	fcc + bcc	bcc (with $B2$-type SRO)
Thermodynamic linear response prediction	SRO driven by Co-Cr pair [very weak tetragonal]	SRO driven by Cr-Al pair	SRO driven by Cr-Mn pair
Phase formation (experiment)	fcc + tetragonal	fcc + bcc + tetragonal	bcc
Chemical distribution (experiment)	Cr-rich phase separation	Cr-rich phase separation	Cr-Mn-Fe and Co-Al based separation

affirm our SRO predictions. For $(CoCrFeMn)_{100-x}Al_x$, a summary of phase stability and SRO predictions from calculations and experiments are listed in the Table I.

IV. CONCLUSION

From first-principles alloy theory, we have predicted the phase stability (formation enthalpy), magnetic stability, and short-range order (SRO) properties of $(CoCrFeMn)_{100-x}Al_x$ ($x \leqslant 20\%$) high-entropy alloys. The theoretical results agree well with our current and other reported experimental data. The $(CoCrFeMn)_{100-x}Al_x$ shows% Al-dependent phase stability as the HEA transforms from fcc ($x = 0$ at.% Al) to bcc ($x > 10$ at.% Al) with two-phase (fcc+bcc*)* region in between. Al (*s-p* orbitals) hybridizing with the transition metals (*d* orbitals) plays a crucial role in structural stability and magnetic, elastic, and chemical properties. The calculated SRO indicate the presence of complex phase at 0 at.% Al, phase separation at 5 at.% Al, and a partially ordered *B*2 phase at 20 at.% Al, in agreement with the experimental data. KKR-CPA electronic structure and SRO offers a quantitative theory-guided design strategy to tailor the structural, chemical, magnetic, and mechanical properties of novel multicomponent alloys by tuning the elements and their alloying. For future design purposes, the global stability (formation energy) and local stability (SRO) can be combined for accelerated alloy design and provide a robust guide to the experimentalist to narrow the search space for desired chemical and mechanical behavior.

[1] J. W. Yeh *et al.*, Nanostructured high-entropy alloys with multiple principal elements: Novel alloy design concepts and outcomes, Adv. Eng. Mater. **6**, 299 (2004).

[2] Y. Zhang *et al.*, Microstructures and properties of high-entropy alloys, Progr. Mater. Sci. **61**, 1 (2014).

[3] M. C. Gao, J.-W. Yeh, P. K. Liaw, and Y. Zhang, *High-Entropy Alloys: Fundamentals and Applications* (Springer, Berlin, 2016).

[4] B. Gludovatz *et al.*, A fracture-resistant high-entropy alloy for cryogenic applications, Science **345**, 1153 (2014).

[5] O. N. Senkov, J. M. Scott, S. V. Senkova, D. B. Miracle, and C. F. Woodward, Microstructure and room temperature properties of a high-entropy TaNbHfZrTi alloy, J. Alloy. Compd. **509**, 6043 (2011).

[6] M. Feuerbacher, M. Heidelmann, and C. Thomas, Hexagonal high-entropy alloys, Mater. Res. Lett. **3**, 1 (2014).

[7] P. F. Yu *et al.*, The high-entropy alloys with high hardness and soft magnetic property prepared by mechanical alloying and high-pressure sintering, Intermetallics **70**, 82 (2016).

[8] M. G. Poletti, G. Fiore, F. Gili, D. Mangherini, and L. Battezzati, Development of a new high entropy alloy for wear resistance: $FeCoCrNiW_{0.3}$ and $FeCoCrNiW_{0.3}+5$ at.% of C, Mater. Design **115**, 247 (2017).

[9] M. A. Hemphill *et al.*, Fatigue behavior of $Al_{0.5}CoCrCuFeNi$ high entropy alloys, Acta Mater. **60**, 5723 (2012).

[10] Y. Zou, J. M. Wheeler, H. Ma, P. Okle, and R. Spolenak, Nanocrystalline high-entropy alloys: A new paradigm in high-temperature strength and stability, Nano Lett. **17**, 1569 (2017).

[11] F. Otto, Y. Yang, H. Bei, and E. P. George, Relative effects of enthalpy and entropy on the phase stability of equiatomic high-entropy alloys, Acta Mater. **61**, 2628 (2013).

[12] G. R. Holcommb, J. Tylczak, and C. Carney, Oxidation of CoFeMnCrNi high entropy alloys, JOM **67**, 2326 (2015).

[13] F. Granberg, K. Nordlund, M. W. Ullah, K. Jin, C. Lu, H. Bei, L. M. Wang, F. Djurabekova, W. J. Weber, and Y. Zhang, Mechanism of Radiation Damage Reduction in Equiatomic Multicomponent Single-Phase Alloys, Phys. Rev. Lett. **116**, 135504 (2016).

[14] K. B. Zhang and Z. Y. Fu, Effects of annealing treatment on phase composition and microstructure of $CoCrFeNiTiAl_x$ high-entropy alloys, Intermetallics **22**, 24 (2012).

[15] L. J. Santodonato *et al.*, Deviation from high-entropy configurations in the atomic distributions of a multi-principal-element alloy, Nat. Commun. **6**, 5964 (2015).

[16] H.-P. Chou, Y.-S. Chang, S.-K. Chen, and J.-W. Yeh, Microstructure, thermophysical and electrical properties in $Al_xCoCrFeNi$ ($0 \leqslant x \leqslant 2$) high-entropy alloys, Mater. Sci. Eng. B **163**, 184 (2009).

[17] F. Otto *et al.*, Decomposition of the single-phase high-entropy alloy CrMnFeCoNi after prolonged anneals at intermediate temperatures, Acta Mater. **112**, 40 (2016).

[18] P. Singh, A. V. Smirnov, and D. D. Johnson, Atomic short-range order and incipient long-range order in high-entropy alloys, Phys. Rev. B **91**, 224204 (2015).

[19] A. Sharma, P. Singh, P. K. Liaw, and D. D. Johnson, and G. Balakrishnan, Atomistic clustering-ordering and high-strain deformation of an $Al_{0.1}CrCoFeNi$ high-entropy alloy, Sci. Rep. **6**, 31028 (2016).

[20] D. D. Johnson, D. M. Nicholson, F. J. Pinski, B. L. Gyorffy, and G. M. Stocks, Density-Functional Theory for Random Alloys: Total Energy within the Coherent-Potential Approximation, Phys. Rev. Lett. **56**, 2088 (1986).

[21] P. Singh, A. V. Smirnov, and D. D. Johnson, Ta-Nb-Mo-W refractory high-entropy alloys: Anomalous ordering behavior and its intriguing electronic origin, Phys. Rev. Mater. **2**, 055004 (2018).

[22] A. Alam and D. D. Johnson, Chemically Mediated Quantum Criticality in $NbFe_2$, Phys. Rev. Lett. **107**, 206401 (2011).

[23] D. D. Johnson, A. V. Smirnov, and S. N. Khan, *MECCA: Multiple-scattering Electronic-structure Calculations for Complex Alloys (KKR-CPA Program, ver. 2.0)* (Iowa State University and Ames Laboratory, Ames, 2015).

[24] D. D. Johnson and F. J. Pinski, Inclusion of charge correlations in calculations of the energetics and electronic structure for random substitutional alloys, Phys. Rev. B **48**, 11553 (1993).

[25] D. D. Johnson, F. J. Pinski, and G. M. Stocks, Self-consistent electronic structure of disordered $Fe_{0.65}Ni_{0.35}$, J. Appl. Phys. **57**, 3018 (1985).

[26] A. L. Marques, M. J. T. Oliveira, and T. Burnus, Libxc: A library of exchange-correlation functionals for density functional theory, Comp. Phys. Commun. **183**, 2272 (2012).

[27] H. J. Monkhorst and J. D. Pack, Special points for Brillouin-zone integrations, Phys. Rev. B **13**, 5188 (1976).

[28] B. L. Györffy, A. J. Pindor, G. M. Stocks, J. Staunton, and H. Winter, A first-principles theory of ferromagnetic phase transitions in metals, J. Phys. F. Met. Phys. **15**, 1337 (1985).

[29] P. Singh *et al.*, Design of high-strength refractory complex solid-solution alloys, npj Comp. Mater. **4**, 16 (2018).

[30] J. B. Staunton, D. D. Johnson, and F. J. Pinski, Compositional short-range ordering in metallic alloys: Band-filling, charge-transfer, and size effects from a first-principles all-electron Landau-type theory, Phys. Rev. B **50**, 1450 (1994).

[31] D. D. Johnson, J. B. Staunton, and F. J. Pinski, First-principles all-electron theory of atomic short-range ordering in metallic alloys: $D0_{22}$- versus $L1_2$-like correlations, Phys. Rev. B **50**, 1473 (1994).

[32] D. D. Johnson, Computation of diffuse intensities in alloys, in *Characterization of Materials*, edited by E. N. Kaufmann (Wiley, New York, 2012), pp. 1–31.

[33] A. Alam, B. Kraczek, and D. D. Johnson, Structural, magnetic, and defect properties of Co-Pt-type magnetic-storage alloys: Density-functional theory study of thermal processing effects, Phys. Rev. B **82**, 024435 (2010).

[34] K. Sato *et al.*, First-principles theory of dilute magnetic semiconductors, Rev. Mod. Phys. **82**, 1633 (2010).

[35] A. Manzoni *et al.*, Phase separation in equiatomic AlCoCrFeNi high-entropy alloy, Ultramicroscopy **132**, 212 (2013).

[36] M. Feuerbacher, E. Wurtz, and C. Thomas, Single-crystal growth of a FeCoCrMnAl high-entropy alloy, Mater. Res. Lett. **5**, 128 (2017).

[37] J. Y. He *et al.*, Effects of Al addition on structural evolution and tensile properties of the FeCoNiCrMn high-entropy alloy system, Acta Mater. **62**, 105 (2014).

[38] A. Marshal, K. G. Pradeep, D. Music, S. Zaefferer, P. S. De, and J. M. Schneider, Combinatorial synthesis of high entropy alloys: Introduction of a novel, single phase, body-centered-cubic FeMnCoCrAl solid solution, J. Alloys Compound **691**, 683 (2017).

[39] T. Yang, Effects of Al addition on microstructure and mechanical properties of AlxCoCrFeNi high-entropy alloy, Mater. Sci. Eng. A **648**, 15 (2015).

[40] B. Cantor, I. T. H. Chang, P. Knight, and A. J. B. Vincent, Microstructural development in equiatomic multicomponent alloys, Mat. Sci. Eng A **375–377**, 213 (2004).

[41] V. L. Moruzzi, J. F. Janak, and A. R. Williams, *Calculated Electronic Properties of Materials* (Pergamon, New York, 1978).

[42] N. A. Zarkevich, T. L. Tan, and D. D. Johnson, First-principles prediction of phase-segregating alloy phase diagrams and a rapid design estimate of their transition temperatures, Phys. Rev. B **75**, 104203 (2007).

[43] K. G. Pradeep, N. Wanderka, P. Choi, J. Banhart, B. S. Murty, and D. Raabe, Atomic-scale compositional characterization of a nanocrystalline AlCrCuFeNiZn high-entropy alloy using atom probe tomography, Acta Mater. **61**, 4696 (2013).